Resonant Microbubble as a Microfluidic Stage for All-Optical Photoacoustic Sensing

Gabriele Frigenti,[1,2,3] Lucia Cavigli,[2,*] Alberto Fernández-Bienes,[4] Fulvio Ratto,[2] Sonia Centi,[2] Tupak García-Fernández,[5] Gualtiero Nunzi Conti,[1,2] and Silvia Soria[2]

[1] *Centro Fermi, Museo Storico della Fisica e Centro Studi e Ricerche "Enrico Fermi", Compendio del Viminale, Piazza del Viminale 1, 00184 Rome RM, Italy*

[2] *Istituto di Fisica Applicata "Nello Carrara", Consiglio Nazionale delle Ricerche, Via Madonna del Piano 10, 50019 Sesto Fiorentino FI, Italy*

[3] *Laboratorio Europeo di Spettroscopia Nonlineare, Università degli Studi di Firenze, Via Nello Carrara 1, 50019 Sesto Fiorentino FI, Italy*

[4] *Facultad de Ingeniería, Universidad Nacional Autónoma de México, Mexico City, Ciudad de México, C.P. 04510, Mexico*

[5] *Universidad Autónoma de la Ciudad de México, Prolongación San Isidro 151, Colonia San Lorenzo Tezonco, Mexico City, Ciudad de México, C.P. 09790, Mexico*

(Received 19 April 2019; revised manuscript received 4 June 2019; published 31 July 2019)

We implement a whispering-gallery-mode microbubble resonator (MBR) as a multifunctional component for all-optical photoacoustic inspection of materials in a platform combining microfluidic design and high sensitivity to spectral absorbance. In our setup, the MBR acts both as the acoustic transducer and as the vial for a sample causing the photoacoustic event, thus dictating its operational frequency and removing any need for impedance-matching media. We challenge our setup in the assessment of the photostability of gold nanorods to demonstrate its validity. We develop a numerical model to qualitatively interpret the experimental signal as a transient shift of the resonance condition of the MBR. Possible implementations of the MBR in photoacoustic sensors are discussed.

DOI: 10.1103/PhysRevApplied.12.014062

I. INTRODUCTION

Whispering-gallery-mode (WGM) resonators have been proposed for a remarkable variety of sensors due to their high Q factor, high resonance peak contrast, and mechanical robustness [1–3]. The main operational principle exploits the change of their resonant condition due to a perturbation in the refractive index of their environment of physical (pressure, temperature, strain, etc.) or biochemical (host-guest recognition) origin [1,2].

Recently, WGM resonators have been proposed as ultrasound detectors with broadband response [4] based on a transient modification of their optical features on impact of a pressure wave that may typically propagate from a remote source through an impedance-matched medium [5–7].

This application is particularly promising in the field of all-optical photoacoustic (PA) imaging, where a need for broadband sensitivity arises from the circumstance that each sample generates its own pattern of acoustic frequencies [8]. Photoacoustics implies the conversion of short optical pulses from a distribution of pigments into a cascade of photothermal and thermoelastic events that produce ultrasound bursts [9]. The detection of the ultrasound signal enables the localization, analysis, or both of the pigments of interest in diverse contexts, such as noninvasive medical imaging [9] as well as nonimaging applications such as flow cytometry [10] and material analysis, more generally [11].

WGM microbubble resonators (MBRs) are a special class of hollow devices typically fabricated by inflating a silica capillary during an arc discharge [12] or intense laser heating [13]. Here we report the implementation of MBRs for nonimaging photoacoustics, where the microfluidic cavity serves to confine the PA source, dictates its power spectrum, and removes the need for impedance-matched media. At variance with the use of integrated resonators as broadband receivers for PA microscopy or tomography [6,8], or that of capillary-based devices to probe an external pressure field [7], our setup takes full advantage of the peculiar features of MBRs and exploits their excellent optical features as well as their high mechanical Q factors. We pursue the sensitive interrogation of ultrasmall fluid volumes to target new devices as compact and portable PA flow cytometers aimed at, for example, liquid biopsy and drug discovery, the development of contrast agents, or the analysis of gases.

*l.cavigli@ifac.cnr.it

II. EXPERIMENTAL SETUP AND METHODS

To demonstrate our device, we conceive an experiment where a MBR is filled with a PA contrast agent, exposed to a short optical pulse from a pump laser triggering the PA event, and coupled to CW light from a probe laser to read the perturbation of one of its WGM resonances induced by the PA transient (see Fig. S1 in Supplemental Material [14]). Therefore, by implementation of a MBR both as the vial containing the sample and as the acoustic transducer, our system is compact, requires no impedance matching material, and takes advantage of the mechanical resonance of the microbubble to achieve high sensitivity.

We decide to use a tapered fiber (taper) to efficiently couple the MBR to the probe laser, and to test gold nanorods (GNRs) as the PA contrast agent, due to their relevance in the realm of PA applications [11]. In particular, the MBR presented in this article is fabricated as in Ref. [12], has a diameter of 430 μm and a capacity of 41 nl, is filled with an aqueous suspension of GNRs (1.3 nM), which are synthesized by the seed-mediated approach described in Refs. [15,16], display a plasmonic resonance around 1064 nm, and have an average size of 70 nm (length) $\times$ 10 nm (diameter).

Our experimental setup is sketched in Fig. 1 and is a practical realization of the concept outlined in Fig. S1 in Supplemental Material [14]. The pump laser is a custom-made pulsed Nd:YAG system (Asclepion Laser Technologies, Jena, Germany; pulse duration 3.3 ns, repetition rate 10 Hz, pulse energy 40 μJ) emitting light at a wavelength of 1064 nm, thus overlapping with the optical absorbance of the GNRs, and focused onto the MBR with a spot diameter of 200 μm. The optical fluence is tuned with a polarizer and monitored with a pyroelectric detector (QE8SP, Gentec-EO, Quebec, QC, Canada).

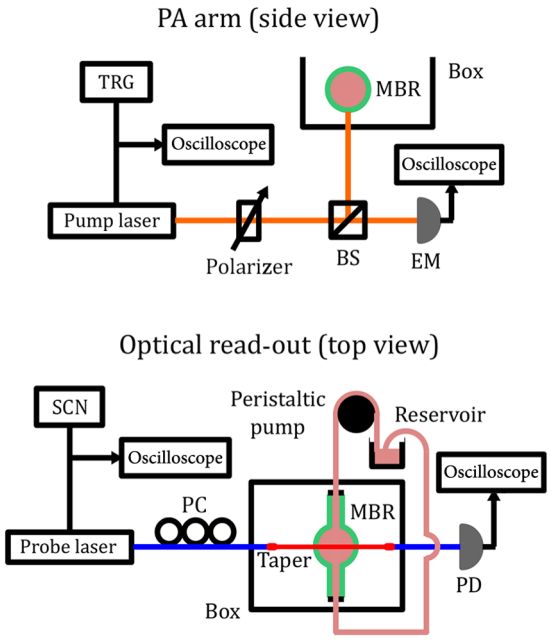

FIG. 1. The experimental setup. BS, beam splitter; EM, pyroelectric detector for energy measurement; PC, polarization controller; PD, photodiode; SCN, waveform generator used to adjust or scan the laser wavelength; TRG, waveform generator used to trigger laser bursts and oscilloscope acquisition.

The probe laser is a low-noise single-frequency system (Koheras ADJUSTICK, NKT Photonics, Birkerød, Denmark; spectral range 1550–1551 nm), and its emission is directed through the taper to an InGaAs photodiode (PDA400, Thorlabs Newton, NJ, USA; bandwidth 10 MHz). A polarization controller is used to optimize the coupling and resonance contrast against the off-resonance transmission, while a voltage ramp from a waveform generator (Keysight 33210A, Agilent Technologies, Santa Clara, CA, USA) is used to adjust or scan the laser wavelength around the WGM resonance. A second waveform generator (Keysight 33220A, Agilent Technologies) is used to trigger both the pump laser and the photodiode acquisition through an RTO1004 digital oscilloscope from Rohde and Schwarz (Munich, Germany). A long-working-distance microscope (custom model, Navitar, Rochester, NY, USA) and a set of micrometer stages are used to optimize the MBR-taper positioning.

The MBR is also connected to a microfluidic circuit powered by a peristaltic pump (Minipuls 3, Gilson, Middleton, WI, USA). The capillary and the taper are placed inside a glass-floor box to isolate the MBR-taper system from disturbing air currents [17].

In practice, after filling the MBR with the aqueous suspension of GNRs, we scan the wavelength of the probe laser to search for a narrow and deep WGM resonance. Figure 2(a) shows the resonance used for the experiments ($Q = 5.2 \times 10^6$, FWHM = 37 MHz), where s_{opt} is the optical transmission through the MBR-coupled taper normalized to its off-resonance value, $\lambda_{\mathrm{half}} = 1550.081$ nm and $\nu_{\mathrm{half}} = c/\lambda_{\mathrm{half}}$ are the wavelength and frequency, respectively, at half minimum, and $\nu - \nu_{\mathrm{half}}$ is the respective detuning. The red curve in Fig. 2(a) is a theoretical fit according to the line shape described in Ref. [18], which demonstrates the assignment of the experimental fringe to a WGM-like resonance. During this scan, the pump laser and peristaltic pump are disabled to prevent mechanical perturbations.

Next, while still recording the optical transmission through the MBR-coupled taper, we set $\lambda = \lambda_{\mathrm{half}}$ and stop scanning, thus obtaining a flat trace [see Fig. 2(b), black curve rendered as a frequency shift of the resonance, as explained below]. The system showed good stability even without active feedback or thermal locking. We then enable the pump laser to trigger the PA generation from the suspension of GNRs and find oscillations of the type shown by the blue curve in Fig. 2(b). To translate these fluctuation in optical transmittance in terms of a frequency shift of the resonance $\delta\nu$, based on

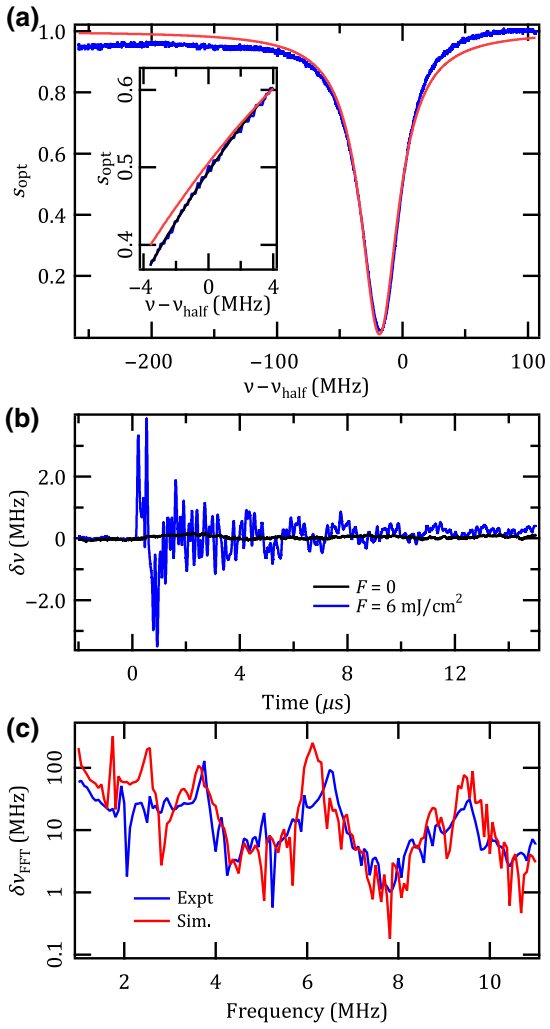

FIG. 2. (a) Resonance used for the experiments (blue curve), along with its theoretical fit based on Ref. [18] (red curve). The inset compares this fit (red curve) with a parabolic fit (black curve) used for interpolation over a smaller range. (b) Frequency shift of the resonance shown in (a) with the pump laser *off* (black curve) or *on* (fluence $F = 6$ mJ/cm^2, blue curve). (c) Comparison between the Fourier spectrum of the experimental signal in (b) (blue curve) and its *ab initio* simulation by finite-element-method modeling (red curve).

the assumption that its line shape remains constant during shifting, we establish and reverse a relationship between s_{opt} and $\nu - \nu_{half}$ through a numerical interpolation of the experimental fringe in Fig. 2(a). We opt for an empirical parabolic fit for analytical convenience.

III. NUMERICAL MODEL

In an attempt to corroborate the hypothesis that $\delta\nu$ is a resonance shift induced by a PA burst originating from the optical absorbance of the GNRs, we develop a finite-element-method (FEM) model of the experimental setup by the use of COMSOL MULTIPHYSICS. The geometry of the simulation features a bulgy segment of glass capillary filled with an aqueous suspension of plasmonic particles, immersed within a continuum of air or water and exposed to an optical pulse impinging the entire bulge. The thickness of the glass wall is retrieved from that of the unperturbed glass capillary according to a spherical approximation [19]. The model recapitulates a complex cascade of steps triggered by an optical pulse (i.e., photothermal conversion from the GNRs, propagation of heat, thermoelastic conversion, propagation of ultrasound [20], and elastic deformation of the walls of the MBR [21,22]) and returns the shift of the resonant condition of the MBR for comparison with the experimental measurable (more details are reported in Supplemental Material [14]). At variance with the quasistatic formulation implemented by other authors [7], our model inherently accounts for the frequency response of the system and so conveys a more-faithful description of its vibration.

The results of the model for the MBR used in this experiment are overlapped in Fig. 2(c) on the Fourier transform of the experimental data shown in Fig. 2(b). In spite of the numerous assumptions and simplifications made within the model and in the description of the WGM resonance, the overall amplitude and the spectral composition of the oscillations point to a remarkable agreement, especially in the range from 2 to 10 MHz. Instead this fidelity tends to break down both at lower frequencies that hang on distal unknowns of the capillary [23] and at higher frequencies that fall outside the bandwidth of the photodiode. Overall, the model succeeds in capturing the essence of the process and highlights the roles of the optical absorbance of the GNRs and the mechanical properties of the microbubble.

To demonstrate that the spectral composition of the signal is a mechanical fingerprint of the microbubble, we perform a series of measurements at different pump fluences. Figure 3(a) shows the power spectra of this series and proves that, despite a remarkable change in amplitude, the frequency composition remains almost identical and displays a sequence of sharp peaks that correspond to the breathing eigenmodes of the microbubble.

Since MBRs display a high mechanical Q factor easily exceeding 10^3 [7,23], our setup provides spectral fingerprints of interest for sensitive detection and suitable for enhancement by, for example, lock-in amplification, in this regard recalling the pulse-echo configuration in use in ultrasonography or ultrasonic testing. By contrast, integrated WGM transducers present a broadband response [24], because their operating principle depends more on a modulation in refractive index rather than a mechanical heterostructure.

Also, to further demonstrate that the resonance shift presented in Fig. 2 largely relates to the optical absorbance of the GNRs, Fig. 3(a) reports the oscillation measured when the MBR contains plain water. With respect to the presence of the GNRs, $\delta\nu$ with plain water maintains a compatible

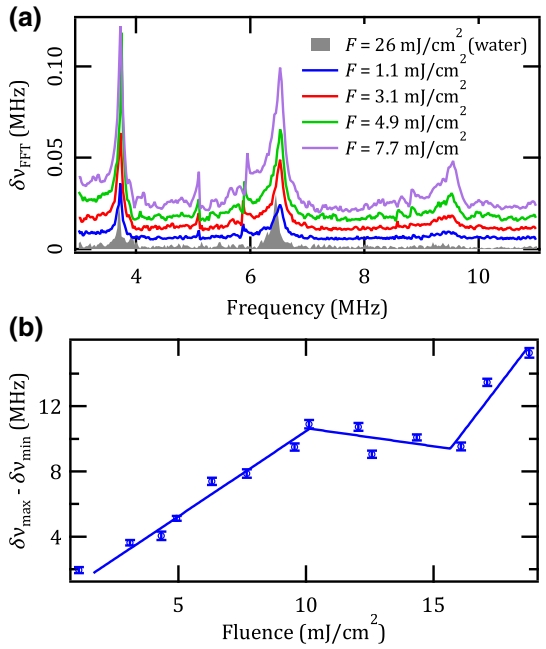

FIG. 3. (a) Frequency spectra of various PA signals recorded at different pump fluences. For comparison, we also show the spectrum of a PA signal measured when the MBR is filled with plain water. Signals are offset by 5 kHz for readability. (b) Peak-to-peak range of the PA signals $\delta\nu$ versus fluence of the pump laser. For each value of the pump fluence, a series of PA traces are recorded and analyzed in terms of the average and standard deviation. The latter are given as error bars to provide an idea of the stability of the measurement. The broken line is a guide for the eye.

spectral composition but much lower amplitude. In particular, in the case of plain water, it takes a pump fluence of around 30 mJ/cm^2 to achieve an amplitude comparable to the PA signal observed at 1 mJ/cm^2 in the presence of the GNRs.

IV. RESULTS AND DISCUSSION

To show a real application case of the MBR system, we challenge the potential of our sensor in a well-known benchmark: the photostability of the GNRs [25]. On excitation with short pulses in a regime of interest for PA applications, GNRs transiently overheat and tend to irreversibly reshape, thus losing their plasmonic fingerprints. In this framework, we previously developed protocols to measure the damage threshold of the GNRs based on their PA response as a function of pump fluence [26]. Here we repeat this experiment by replacing the standard piezoelectric transducer with the MBR setup and recording the amplitude of the PA signals [defined as peak-to-peak range equivalent to max $(\delta\nu)$ − min $(\delta\nu)$] as a function of pump fluence. The resulting plot [Fig. 3(b)] shows the typical trend featuring three distinct regimes associated with two changes in slope [27]; that is, an earlier cutoff around 10 mJ/cm^2 corresponding to the damage threshold of the GNRs and then a later cutoff around 20 mJ/cm^2 corresponding to the onset of nonlinear processes as photocavitation [27].

This result proves that a MBR-based PA gauge may be used in the development and assessment of optical contrast agents. With respect to standard transducers, the advantages include high sensitivity to small volumes and operability in air rather than water. Regarding the latter feature, we use our numerical model to compare the predicted performance of a MBR transducer in the air-coupled configuration presented in this work and a virtual-water-coupled alternative where the microbubble is immersed in water, as a typical piezoelectric transducer. The results are reported in Fig. 4(a) and show that, with respect to the

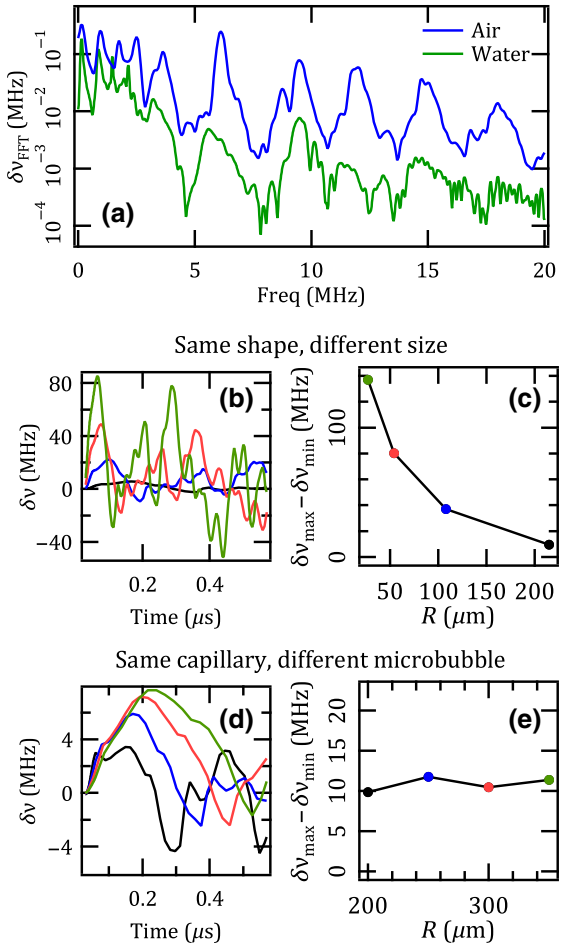

FIG. 4. Expected behavior of alternative MBR configurations simulated by the use of our numerical framework. (a) Comparison of the frequency spectra of simulated PA signals for a MBR placed in air (blue curve) and in water (green curve). Simulated PA signals (b),(d) and amplitudes (c),(e) for MBRs of the same shape and different size (b),(c) or obtained by keeping the same glass capillary and varying both the shape and the size according to Ref. [23] (d),(e). The same color codes are used in (c),(e) as in (b),(d), respectively.

air-coupled signal, the water-coupled counterpart displays a substantial attenuation of higher-frequency components, probably due to the stiffness of water. Therefore, the possibility to work in air rather than water is not only more convenient but also more desirable in terms of sensitivity and specificity.

With the assumption that the FEM model is adequate to capture the principal trends of our sensor and in pursuit of future directions to increase sensitivity, we simulate the effect of miniaturization. The results are reported in Figs. 4(b) and 4(c) for systems scaled down with respect to the experimental configuration ($R_{\mathrm{expt}} = 215\ \mu$m) but with no change in shape. In other words, we simulate uniformly miniaturized versions of the device, comprising the MBR and the host capillary. Practically, this may be achieved by blowing a MBR from silica capillaries of smaller size, as would be commercially available or manufacturable in house by stretching. We keep the same pump energy as well as the same particle concentration. The curves show that miniaturization may be an effective direction to increase sensitivity.

On the other hand, Figs. 4(d) and 4(e) compare the PA signals and amplitudes for MBRs realized on the same glass capillary, but differing in diameter within a range of experimental feasibility [23]. In practice, at variance with Figs. 4(b) and 4(c), the microbubbles in Figs. 4(d) and 4(e) connect to a stump of the same size, and so their wall thickness becomes smaller as their diameter becomes larger [23]. Figure 4(e) shows that the PA response of these MBRs has a similar amplitude and no clear trend, which leaves little room for optimization when the same glass capillary is used and suggests that the results presented in this article are robust with respect to the fabrication variability from microbubble to microbubble. Instead, the frequency composition of these oscillations exhibits subtle variations that may be exploited for multiplexing.

We finally attempt an analysis of the detection limit of our platform. From Fig. 3(b), we start from a signal amplitude of about 10 MHz for a pump fluence limited by the damage threshold of the GNRs and for a particle concentration corresponding to an optical density $\mu \sim 4\ \mathrm{cm}^{-1}$. The linearity of all underlying processes would enable an at least 100-fold dilution of the sample before the noise level under 100 kHz is reached [see Fig. 2(b)], corresponding to a detection limit below 3×10^5 particles. Given the simulations in Fig. 3(c) and assuming the same noise level, for the smallest MBR with a capacity of 0.64 nl, we predict a detection limit of around 3000 particles within the damage threshold of the GNRs.

In the context of general interest in photoacoustics such as blood and its oxygen saturation [28,29], with $\mu \sim 112\ \mathrm{cm}^{-1}$ at a wavelength of 500 nm for a typical concentration of red cells of $5 \times 10^6\ \mu\mathrm{l}^{-1}$ [30], the figures found for the GNRs translate into a detection limit of around 70 red cells for the experimental configuration and less than a single cell for the smallest size. By replacing the constraint given by the damage threshold of the GNRs with that of red cells, which is larger by more than 3 orders of magnitude [31], we would readily achieve sensitivity below 1% of a single cell, which would probably enable accurate quantification of its oxygenation by PA spectroscopy.

V. CONCLUSIONS

In conclusion, we implement a WGM microbubble resonator as an optical transducer in an all-optical PA platform suitable for the analysis of fluid samples. Our experimental configuration features the microbubble resonator in the double role of an ultrasound sensor and a microvial, thus enabling the PA inspection of submicroliter samples without the need for impedance-matching media.

We interpret the optical read-out signal of the transducer through a FEM model that comprises all relevant steps, starting from the optical absorption of the PA contrast agent and ending with the resonance shift associated with the structural deformation of the microbubble. We find that our system supports a set of operating frequencies that constitute a mechanical fingerprint of the microbubble and provide high sensitivity.

To validate and assess the performance of this device, we perform a quantitative characterization of the photophysical properties of gold nanorods at a particle concentration of a few nanomoles per liter, which is a representative case in photoacoustics.

In perspective, further miniaturization of this platform promises better performance with higher sensitivity easily down to the level of a single red cell, which may pave the way to a new generation of nonimaging PA devices for applications in biosensing, flow cytometry, and material science.

ACKNOWLEDGMENTS

We thank Franco Cosi from Istituto di Fisica Applicata "Nello Carrara" for manufacturing the tapered fibers. We acknowledge funding from the CNR-CONACyT bilateral project "All optical morphogenesis of nanostructures characterized by photoacoustic microscopy" (2017–2019, CONACyT Grant No. 278094) and partial funding from the Centro Fermi project MiFo.

[1] A. Chiasera, Y. Dumeige, P. Féron, M. Ferrari, Y. Jestin, G. Nunzi Conti, S. Pelli, S. Soria, and G. Righini, Spherical whispering gallery modes microresonators, Laser Photonics Rev. **4**, 457 (2010).

[2] A. Watkins, J. Ward, Y. Wu, and S. N. Chormaic, Single-input spherical microbubble resonator, Opt. Lett. **36**, 2113 (2011).

[3] M. R. Foreman, J. D. Swaim, and F. Vollmer, Whispering gallery mode sensors, Adv. Opt. Photon. **7**, 168 (2015).

[4] C. Zhang, S. Chen, T. Ling, and L. J. Guo, Review of imprinted polymer microrings as ultrasound detectors: Design, fabrication, and characterization, IEEE Sens. J. **15**, 3241 (2015).

[5] B. Dong, H. Li, Z. Zhang, K. Zhang, S. Chen, C. Sun, and H. F. Zhang, Isometric multimodal photoacoustic microscopy based on optically transparent micro-ring ultrasonic detection, Optica **2**, 169 (2015).

[6] S.-L. Chen, L. J. Guo, and X. Wang, All-optical photoacoustic microscopy, Photoacoustics **3**, 143 (2015).

[7] K. H. Kim, W. Luo, C. Zhang, C. Tian, L. J. Guo, X. Wang, and X. Fan, Air-coupled ultrasound detection using capillary-based optical ring resonators, Sci. Rep. **7**, 109 (2017).

[8] G. Wissmeyer, M. A. Pleitez, A. Rosenthal, and V. Ntziachristos, Looking at sound: Optoacoustics with all-optical ultrasound detection, Light.: Sci. Appl. **7**, 53 (2018).

[9] S. Manoharand and D. Razansky, Photoacoustics: A historical review, Adv. Opt. Photon. **8**, 586 (2016).

[10] D. A. Nedosekin, T. Fahmi, Z. A. Nima, J. Nolan, C. Cai, M. Sarimollaoglu, E. Dervishi, A. Basnakian, A. S. Biris, and V. P. Zharov, Photoacoustic flow cytometry for nanomaterial research, Photoacoustics **6**, 16 (2017).

[11] J. Weber, P. C. Beard, and S. E. Bohndiek, Contrast agents for molecular photoacoustic imaging, Nat. Methods **13**, 639 (2016).

[12] S. Berneschi, D. Farnesi, F. Cosi, G. Nunzi Conti, S. Pelli, G. C. Righini, and S. Soria, High Q silica microbubble resonators fabricated by arc discharge, Opt. Lett. **36**, 3521 (2011).

[13] M. Sumetsky, Y. Dulashko, and R. S. Windeler, Optical microbubble resonator, Opt. Lett. **35**, 898 (2010).

[14] See Supplemental Material at http://link.aps.org/supplemental/10.1103/PhysRevApplied.12.014062 for additional information on the experimental setup and the COMSOL MULTIPHYSICS simulation.

[15] L. Vigdermanand and E. R. Zubarev, High-yield synthesis of gold nanorods with longitudinal spr peak greater than 1200 nm using hydroquinone as a reducing agent, Chem. Mater. **25**, 1450 (2013).

[16] L. Cavigli, S. Centi, C. Borri, P. Tortoli, I. Panettieri, I. Streit, D. Ciofini, G. Magni, F. Rossi, S. Siano, F. Ratto, and R. Pini, 1064-nm-resonant gold nanorods for photoacoustic theranostics within permissible exposure limits, J. Biophotonics, e201900082 (2019).

[17] A. Cosci, S. Berneschi, A. Giannetti, D. Farnesi, F. Cosi, F. Baldini, G. Nunzi Conti, S. Soria, A. Barucci, G. Righini, and S. Pelli, Resonance frequency of optical microbubble resonators: Direct measurements and mitigation of fluctuations, Sensors **16**, 1405 (2016).

[18] G. Frigenti, M. Arjmand, A. Barucci, F. Baldini, S. Berneschi, D. Farnesi, M. Gianfreda, S. Pelli, S. Soria, A. Aray, Y. Dumeige, P. Féron, and G. Nunzi Conti, Coupling analysis of high q resonators in add-drop configuration through cavity ringdown spectroscopy, J. Opt. **20**, 065706 (2018).

[19] A. Cosci, F. Quercioli, D. Farnesi, S. Berneschi, A. Giannetti, F. Cosi, A. Barucci, G. N. Conti, G. Righini, and S. Pelli, Confocal reflectance microscopy for determination of microbubble resonator thickness, Opt. Express **23**, 16693 (2015).

[20] L. V. Wang, *Photoacoustic Imaging and Spectroscopy* (CRC Press, Boca Raton, 2009).

[21] P. M. Morseand and K. Uno Ingard, *Theoretical Acoustics* (Princeton University Press, Princeton, 1986).

[22] A. Safariand and E. K. Akdoğan, *Piezoelectric and Acoustic Materials for Transducer Applications* (Springer, New York, 2008).

[23] X. Rosello Mecho, D. Farnesi, G. Frigenti, A. Barucci, A. Fernandez Bienes, T. Garcia Fernandez, F. Ratto, M. Delgado Pinar, M. V. Andrés, G. Nunzi Conti, and S. Soria, Parametrical optomechanical oscillations in phoxonic whispering gallery mode resonators, Sci. Rep. **9**, 7163 (2019).

[24] A. Maxwell, S. Huang, T. Ling, J. Kim, S. Ashkenazi, and L. J. Guo, Polymer microring resonators for high-frequency ultrasound detection and imaging, IEEE J. Sel. Top. Quantum Electron. **14**, 191 (2008).

[25] L. Cavigli, A. Cini, S. Centi, C. Borri, S. Lai, F. Ratto, M. de Angelis, and R. Pini, Photostability of gold nanorods upon endosomal confinement in cultured cells, J. Phys. Chem. C **121**, 6393 (2017).

[26] L. Cavigli, F. Tatini, C. Borri, F. Ratto, S. Centi, A. Cini, B. Lelli, P. Matteini, and R. Pini, Preparation and photoacoustic analysis of cellular vehicles containing gold nanorods, J. Vis. Exp. **111**, e53328 (2016).

[27] L. Cavigli, F. Micheletti, P. Tortoli, S. Centi, S. Lai, C. Borri, F. Rossi, F. Ratto, and R. Pini, Light activated microbubbles for imaging and microsurgery, Proc. SPIE **10064**, 1006457 (2017).

[28] V. Gnyawali, E. M. Strohm, J.-Z. Wang, S. S. H. Tsai, and M. C. Kolios, Simultaneous acoustic and photoacoustic microfluidic flow cytometry for label-free analysis, Sci. Rep. **9**, 1585 (2019).

[29] F. Ratto, L. Cavigli, C. Borri, S. Centi, G. Magni, M. Mazzoni, and R. Pini, Hybrid organosilicon/polyol phantom for photoacoustic imaging, Biomed. Opt. Express **10**, 3719 (2019).

[30] S. A. Prahal, https://omlc.org/spectra/hemoglobin/.

[31] V. P. Zharov, E. I. Galanzha, E. V. Shashkov, N. G. Khlebtsov, and V. V. Tuchin, In vivo photoacoustic flow cytometry for monitoring of circulating single cancer cells and contrast agents, Opt. Lett. **31**, 3623 (2006).